GC-IRS13E - AN ASSOCIATION OF THREE PUZZLING EARLY-TYPE STARS

T.K. Fritz[1], S. Gillessen[1], K. Dodds-Eden[1], F. Martins[2], H. Bartko[1], R. Genzel[1,3], T. Paumard[4], T. Ott[1], O. Pfuhl[1], S. Trippe[5], F. Eisenhauer[1], D. Gratadour[4],

Draft version March 10, 2010

ABSTRACT

We present a detailed analysis of high resolution near-infrared imaging and spectroscopy of the potential star cluster IRS13E very close to the massive black hole in the Galactic Center. We detect 19 objects in IRS13E from Ks-band images, 15 of which are also detected reliably in H-band. We derive consistent proper motions for these objects from the two bands. Most objects share a similar westward proper motion. We characterize the objects using spectroscopy (1.45 to 2.45 μm) and (narrow-band) imaging from H- (1.66 μm) to L'-band (3.80 μm). Nine of the objects detected in both Ks- and H-band are very red, and we find that they are all consistent with being warm dust clumps. The dust emission may be caused by the colliding winds of the two Wolf-Rayet stars in the cluster. Three of the six detected stars do not share the motion or spectral properties of the three bright stars. This leaves only the three bright, early-type stars as potential cluster members. It is unlikely that these stars are a chance configuration. Assuming the presence of an IMBH, a mass of about 14000 $M_\odot$ follows from the velocities and positions of these three stars. However, our acceleration limits make such an IMBH nearly as unlikely as a chance occurrence of such a star association. Furthermore, there is no variable X-ray source in IRS13E despite the high density of dust and gas. Therefore, we conclude that is unlikely that IRS13E hosts a black hole massive enough to bind the three stars.

Subject headings: infrared: stars — Galaxy: center

1. INTRODUCTION

The innermost parsec of the Galaxy hosts the supermassive black hole (SMBH) Sgr A* (Schödel et al. 2002; Ghez et al. 2003), accompanied by a population of young WR/O-stars (Forrest et al. 1987; Allen et al. 1990; Krabbe et al. 1991; Genzel et al. 1996). Most of these stars reside in one or two disk-like structures (Genzel et al. 2003; Paumard et al. 2006; Lu et al. 2009; Bartko et al. 2009). A group of at least three bright stars called IRS13E at a distance of $3.5'' = 0.13$ pc from Sgr A* is of special interest. This group has a diameter of about $0.5''$. Maillard et al. (2004) identified two of the stars, E2 and E4, from their emission lines as early-type stars. In addition they identified four other early-type stars in IRS13E from broad-band SED fitting. The four brightest stars share a common proper motion (Ott 2002). Maillard et al. (2004) concluded without using a statistical test that such an association of young stars cannot be a coincidence. From the radial velocities of two of the stars they estimated a cluster mass of at least 750 $M_\odot$ if the two stars are bound. This mass is higher than the stellar mass seen in IRS13E. They explained the additional mass by the presence of an intermediate mass black hole (IMBH).

In the simulations of stellar clusters of Portegies Zwart & McMillan (2002) the core of a dense cluster collapses and forms an IMBH. Such an IMBH would be necessary, if IRS13E were an inspiraling cluster that survives the infall into the Galactic Center (GC) and reaches the central parsec before disintegrating (Hansen & Milosavljević 2003). A cluster without central mass would be disrupted (Gerhard 2001) by the tidal forces of the SMBH.

Schödel et al. (2005) measured the proper motions of the four brightest sources more accurately and estimated that the cluster has a mass of about 50000 $M_\odot$ if it is gravitationally bound. According to these authors, an IMBH of this mass is unlikely, mainly because of the lack of radio and X-ray emission in IRS13E, despite the presence of a lot of dust. Instead, they suggested that it is a cluster with a smaller IMBH in the process of dissolution.

Paumard et al. (2006) identified the spectral types of the three brightest early-type stars. In addition, they measured the stellar surface density around IRS13E on a deconvolved H-band image. Inside a radius of $0.30''$, the core of IRS13E, they found at least twelve stars. Furthermore, they found an over-density out to $0.68''$ which has a total significance of 4.5σ. They concluded that IRS13E is a cluster. Given that velocities had been measured for only four of the stars, Paumard et al. (2006) argued that the total velocity dispersion could be small. Then no dark mass is needed to explain IRS13E. Trippe et al. (2008) measured the velocities of the stars between $0.30''$ and $0.68''$. The velocities of most of these stars are different from the stars in the center. Therefore most of them are not cluster members and thus the overdensity is less significant compared to Paumard et al. (2006).

Accordingly, the nature of IRS13E is still a matter of debate. This is largely because the proper motions and the nature of the member objects are known only for very few sources in the core with a radius of about $0.3''$. In

[1] Max Planck Institut für Extraterrestrische Physik, Postfach 1312, D-85741, Garching, Germany; tfritz@mpe.mpg.de
[2] GRAAL-CNRS, Université Montpellier II -UMR5024, Place Eugme Bataillon, F-34095, Montpellier, France
[3] Department of Physics, University of California, Berkeley, 366 Le Comte Hall, Berkeley, CA 94720-7300
[4] LESIA, Observatoire de Paris, CNRS, UPMC, Université Paris Diderot; 5 Place Jules Janssen, 92190 Meudon, France
[5] Institute de radioastronomie Millimétrique, 300 rue de la Piscine, F-38406 Grenoble, France

particular, it is not clear whether all objects identified by previous works actually are stars. In this paper we analyze seven years of imaging data (presented in section 2). We identify 19 objects in the core of IRS13E, for all of which we can measure proper motions (section 3). For the brightest sources E1 and E2, we obtain acceleration limits which start to to constrain the nature of IRS13E (section 3). From H- to L'-band photometry and H+K-band spectra we constrain the nature of the objects (section 4). In Section 5 we calculate the probability that there is an IMBH in IRS13E given our data. Section 6 considers other data in a more qualitative fashion and theoretical models. Finally we summarize and conclude in Section 7. We assume a distance to the GC of $R_0 = 8$ kpc (Reid 1993) and a mass of the SMBH of $M = 4 \times 10^6 M_\odot$ (Ghez et al. 2008; Gillessen et al. 2009).

2. DATASET

This study uses seven years of adaptive optics based imaging data and spectroscopic data obtained with an integral field spectrograph in 2004 and 2009. This section briefly describes our data set.

2.1. *NACO*

We obtained images with NAOS/CONICA (NACO) mounted on UT4 at the VLT (Lenzen et al. 2003; Rousset et al. 2003)[6]. The camera CONICA, together with the adaptive optics (AO) system NAOS, achieves diffraction limited images in the near-infrared. For this study, we use mainly the 13 mas/pixel image scale. On this scale, the point spread function (PSF) is oversampled. This is suited better for highly crowded fields than a strict Nyquist sampling (Trippe et al. 2009).

For source detection and astrometry, we use data from nearly every observing run from April 2002 to May 2009, excluding only the worst 10% of data. In total, our sample consists of 37 H-, 74 Ks- and 5 L'-band images.

We base the broad-band photometry on four H-, four Ks- and three L'-band images that were of particularly good quality. Furthermore, we use four narrow-band images for photometry, which we obtained at $2.06\,\mu$m, $2.24\,\mu$m (12-06-2004), $2.17\,\mu$m and $2.33\,\mu$m (13-06-2004).

All images are flat-fielded, bad pixel corrected and sky subtracted. In addition, we correct images in which saturation is important for the nonlinearity of the detector. We combine single images of typically 30 seconds exposure into stacked images. Because the faint additional sources in IRS13E lie in the PSF halos of the bright stars, the prime goal of the data reduction is to obtain the highest Strehl ratio possible for each data set, even at the cost of smaller total exposure (Fritz et al. 2010). For this reason, we select frames of good quality only.

2.2. *SINFONI*

Spectroscopy allows one to obtain a secure identification of spectral types and to measure radial velocities. We use spectra obtained with the integral field spectrometer SINFONI (Eisenhauer et al. 2003;

Bonnet et al. 2003) at UT4 of the VLT[7]. We analyze high-quality H+K-band laser and natural guide star data from May 21 and 23, 2009. The data from the latter date have a Strehl ratio of 28% at $2.18\,\mu$m and a total of $2400\,s$ exposure. The spatial sampling is 12.5 mas × 25 mas pixel^{-1}, the spectral resolution is 1500. We apply the standard data reduction for SINFONI data, including detector calibrations (such as bad pixel correction, flat-fielding and distortion correction) and cube reconstruction. The wavelength scale is calibrated by means of emission line lamps and finetuned with atmospheric OH lines. The remaining uncertainty corresponds to typically (less than) 10 km/s.

3. ASTROMETRY

3.1. *Image processing*

One of the main aims of this study is to characterize the faint objects in the core of IRS13E, the velocities of which are unknown. We base our analysis on deconvolution of the images, which requires the determination of the PSF for each image.

For creating a PSF we use starfinder version 1.2 (Diolaiti et al. 2000). We extract the PSF from ten to 15 stars brighter than $m_{Ks} = 13.5$ and symmetrically distributed around IRS13E up to a distance of 4". We then use the Lucy-Richardson algorithm (Lucy 1974). Depending on the image quality, we choose between 6000 and 20000 iterations. This number also correctly handles extended sources. For example, the extended object IRS2L (Blum et al. 1996) contains only one maximum after deconvolution, and a large fraction of the flux remains detached from the central maximum. We do not smooth the result of the deconvolution at all and find stellar positions by centroids around local maxima.

We deconvolve all H- and Ks-band images. We then select by visual inspection the images for the subsequent analysis, on which at least some of the fainter objects are visible. These are 61 Ks-band images and 18 H-band images. This subjective quality selection is nearly identical to a Strehl ratio cut of 9% in both bands.

3.2. *Object detection*

Some care is needed to distinguish between real and spurious sources since we are dealing with a crowded field imaged at the diffraction limit. Our procedure is as follows. We start by measuring the positions of the local maxima on the quality-selected, deconvolved images. We treat each frame individually, such that we can neglect maxima that are unlikely to correspond to a real source. These are for example maxima only marginally brighter than the noise floor or the background from the minispiral, or maxima that apparently are affected by deconvolution artifacts.

We consider an object to be well-detected if it is found in either at least three images in both H- and Ks-band, or in at least ten Ks-band images. This is a robust criterion, since the objects are present in images that sample a wide range of PSF shapes. According to these criteria, we detect 19 sources in the core ($r \lesssim 0.3''$) of IRS13E (Figure 1). The rms position deviation of these sources to a linear fit to the Ks-band data is 7 mas in median.

---

[6] We use NACO data from ESO programs 70.B-0649, 71.B-0077, 71.B-0078, 71.B-0365, 072.B-0285, 073.B-0084, 073.B-0085, 073.B-0665, 073.B-0775, 075.B-0093, 077.B-0014, 078.B-0136, 179.B-0261, 179.B-0932, 183.B-0100.

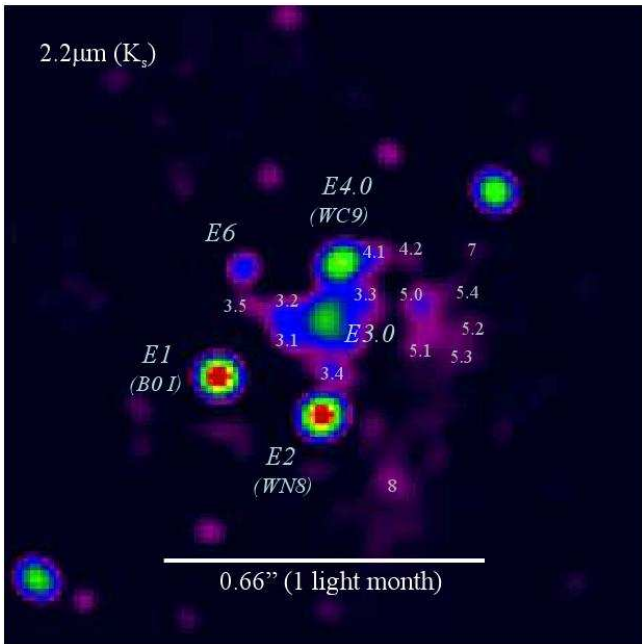[7] We use SINFONI data from ESO program 183.B-100.

FIG. 1.— Coadd of four Lucy-deconvolved Ks-images of IRS13E in 2008, smoothed with a Gaussian with a FWHM of 2 pixels. The intensity scale is logarithmic. The sources which we consider real are marked with numbers. Nearly all of these objects are also found in H-band images.

Thus all measured positions of the 19 sources lie within an area of $4000\,\mathrm{mas}^2$, only 1/50 of the area of the cluster core. Therefore the sources are not random fluctuations.

We test by means of simulated images that indeed our detection procedure is robust. Using a variety of PSFs we find that it is only possible to continue to obtain the same sources after deconvolution if indeed these sources had been put into the simulation.

3.3. Proper motions

Given the pixel positions, we go to an astrometric coordinate system by constructing a full linear transformation using ten bright, isolated stars from the astrometric list of Trippe et al. (2008) close to IRS13E. Proper motions are in turn obtained by fitting the positions as a function of time by linear functions. Since we are using many position measurements for the fitting, we simply use an unweighted fit. The errors for any given objects are set to the scatter of the data around the linear motion model. For the fit, 5σ-outliers are rejected. There are only two such cases in H and Ks for all the objects.

In the L'-band the exclusion of 5σ outliers becomes important, and the errors are mostly larger. The L'-band velocities differ significantly from the velocities obtained from the other bands for the three brightest stars. The differences can be as large as 16σ and $2.5\,\mathrm{mas/yr}$. The differences are caused by L'-band dust emission that is important around IRS13E. The L'-band velocities are less useful and we neglect them in our analysis.

The proper motion fits are presented in table 1 and figure 13. For the bright stars E1, E2 and E4.0 we also fit second order polynomials to the stellar positions as a function of time to test for accelerations. The accuracy reached for the three brightest stars starts to constrain the mass of a putative IMBH.

For most objects the astrometry from H- and Ks-band is consistent. The biggest discrepancy happens for E4.0 that shows a velocity difference of 16 km/s or $3.7\,\sigma$ in R.A. The value for the R.A.-velocity in Ks lies between the velocities obtained from H- and L'-band data. Therefore, we assume that dust perturbs the position of this star also in Ks-band, not only in L'-band. Consequently we only use the astrometry from H-band data for this star, and we also don't trust the marginally significant acceleration in Dec. direction.

Similarly, for the faint or confused objects (E3, E4.1, E4.2, E5, E7, E8) we adopt the measurements derived from the band where the source is more prominent compared to the local background level. For the relatively blue objects E3.5, E4.0 and E4.2 this is the H-band, for the other ones Ks-band. For the unconfused objects E1, E2 and E6 we use the weighted average of the two bands.

4. CHARACTERIZATION OF THE OBJECTS

In order to address the question of whether IRS13E hosts an IMBH, it is important to know the nature of its constituent objects. Only stars can be used reliably as fiducial tracers for a gravitational potential, and an overdensity of objects compared to the stellar background is only meaningful if these are actually stars. In this section we first describe the combined photometric and spectroscopic method to construct a SED. Then we use it to constrain the nature of the individual objects. We present the results for the most important objects here and leave for the appendix a description of the details of the method and the results for the remaining objects.

4.1. Method

For each object we construct a spectral energy distribution (SED), ideally ranging from H- to L'-band. For this we use broad- and narrow-band images plus the two spectro-imaging data cubes in the combined H+K-band.

Where possible, we identify the objects in the SINFONI data by their spectral features as late- or early-type stars. In this way we show that E1, E2, E4.0 and E6.0 are stars. For the other objects we construct SEDs from a deconvolved SINFONI cube and the narrow-band imaging data (appendix A). We then estimate whether a stellar component is required to explain the SED.

Following the approach of Maillard et al. (2004), we consider models composed of an extinction parameter and either one or two temperatures corresponding to a star and dust. We derive the temperature of the stellar component from the lines in the spectrum when possible. Otherwise we assume a temperature of $9480\,\mathrm{K}$ (corresponding to the spectral type A0V) for the star. This is sufficient, since the shape of the SEDs in our wavelength range depends only weakly on the assumed temperature for the stellar component of the SED model.

We use the extinction law of Draine (1989) shortward of Brackett-β and $A_{Ks}/A_{L'} = 1.75$ (Lutz et al. 1996). When fitting models to the less well measured SEDs, we only use extinction values that differ less than $\Delta A_{Ks} = 0.3$ from the value for E1. This range seems adequate given the work of Schoedel et al. (2009) and our result does not depend strongly on this assumption. We neglect the nebular lines originating from the interstellar gas. At our precision their contributions to the flux are negligible

TABLE 1
PROPER MOTIONS AND ACCELERATION LIMITS OF THE OBJECTS IN IRS13E

Object	band	R.A. [as]	$v_{R.A.}$ [km/s]	Dec. [as]	$v_{Dec.}$ [km/s]	$a_{R.A.}$ [$\mu as/yr^2$]	$a_{Dec.}$ [$\mu as/yr^2$]
E1	H and Ks	-2.95825	-142.5 ± 1.3	-1.64478	-105.5 ± 0.7	22 ± 20	11 ± 14
E2	H and Ks	-3.17094	-249.2 ± 1.1	-1.73176	23 ± 0.7	20 ± 19	-14 ± 16
E3.0	Ks	-3.18432	-82 ± 9	-1.52843	8 ± 9		
E3.1	Ks	-3.12602	19 ± 39	-1.56207	19 ± 43		
E3.2	Ks	-3.09296	-74 ± 38	-1.52515	84 ± 24		
E3.3	Ks	-3.25190	-262 ± 17	-1.4905	2 ± 15		
E3.4	Ks	-3.20266	-97 ± 20	-1.63206	-23 ± 27		
E3.5	H	-3.02596	-12 ± 51	-1.50076	-126 ± 48		
E4.0	H	-3.21042	-227 ± 4	-1.40868	26 ± 4	80 ± 70	-30 ± 80
E4.1	Ks	-3.28090	-211 ± 21	-1.40982	206 ± 18		
E4.2	H	-3.36377	-25 ± 43	-1.4015	-80 ± 27		
E5.0	Ks	-3.38164	-136 ± 12	-1.50247	175 ± 14		
E5.1	Ks	-3.39144	-87 ± 38	-1.56858	42 ± 34		
E5.2	Ks	-3.47362	-340 ± 38	-1.54073	3 ± 28		
E5.3	Ks	-3.45754	-139 ± 39	-1.60706	163 ± 30		
E5.4	Ks	-3.44586	-68 ± 38	-1.46880	30 ± 34		
E6	H and Ks	-3.01009	-133 ± 7	-1.42346	23 ± 7		
E7	Ks	-3.49489	-227 ± 29	-1.39103	167 ± 28		
E8	Ks	-3.31966	-118 ± 18	-1.86638	95 ± 20		

NOTE. — The positions are given for 12-05-2005 and are measured relative to Sgr A*.

For the bright early-type stars we have well-measured spectra such that an explicit comparison with atmosphere models becomes viable. We use the code CM-FGEN (Hillier & Miller 1998) to derive the main parameters of the stellar atmospheres of E1, E2 and E4.0. The code computes non-LTE atmosphere models including wind and line-blanketing. We proceed as in Martins et al. (2007). A slight improvement in the method is the use of iterations on the hydrodynamic structure to ensure a better consistency between the atmosphere model per se and the density/velocity structure (Martins et al. 2009). The derived stellar parameters rely on line ratios and photometry. In addition, we derive the extinction by fitting the shape of the infrared SEDs. Hence, for each star, we have computed several models with different luminosities and looked for the best combination of luminosity, extinction and dust emission.

4.2. Individual Objects

This section describes the nature of the most important objects in IRS13E. For a description of the other objects, see appendix B. Table 2 presents the values of the model parameters for all objects, for which our data allow an identification.

4.2.1. IRS13E3.0

We resolve E3 on the deconvolved images into six stable sources and name them E3.0, E3.1, E3.2, E3.3, E3.4 and E3.5. This section describes the brightest component E3.0, which likely is extended or multiple at our resolution. Its flux increases significantly by 0.25 mag between 2002 and 2008 in H- and Ks-bands, the main increase happens between 2004 and 2006. This in not caused by confusion.

We extract a spectrum from the SINFONI data at the position of E3.0, see Figure 3. This spectrum also contains flux from the other five E3 sources and the extended background, but E3.0 completely dominates due to its brightness.
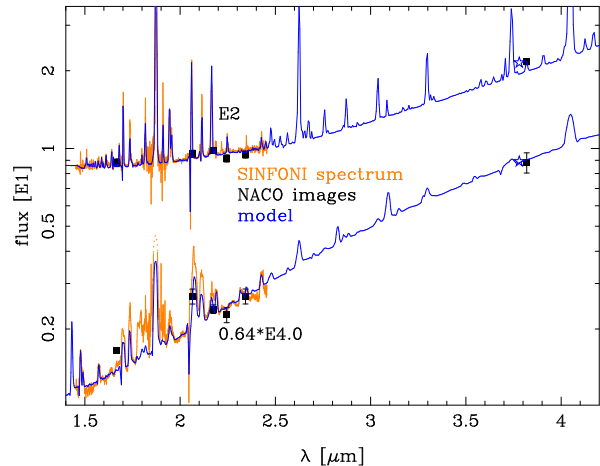

FIG. 2.— H+K-band spectrum and photometry of the two WR-stars in IRS13E: E2 (WN8) and E4.0 (WC9). We fit full atmosphere models plus blackbodies with dust-like temperatures to the observed spectra and L'-band flux points. The asterisks denote the average flux of the models in L'-band, to which the measured flux needs to be compared.

No stellar line (absorption line, or broader emission line) is visible in E3.0, but many of narrow emission lines from H, Fe and He are present. Nearly all these lines are very similar to the surrounding nebular background. A few lines like H_2 at $2.122\,\mu m$ and $2.223\,\mu m$ are only present in the background. Most identifiable lines (HI, HeI, FeII, FeIII) are known from the minispiral (Lutz et al. 1993) or are other hydrogen lines.

Stellar absorption lines of fainter stars are likely too weak for being detectable against the strong narrow emission lines of the surrounding gas. However, that there are any WR-stars in E3.0 seems unlikely, since the strong, broad emission lines of such stars would be visible. For example, E4.0 (a WC9 star) scaled down to $m_{Ks} = 15$ would be detectable against the narrow emission lines. Given that a WR-star cannot be fainter than $m_{Ks} = 16.5$ (Crowther 2007), only a few types of WR-stars could be
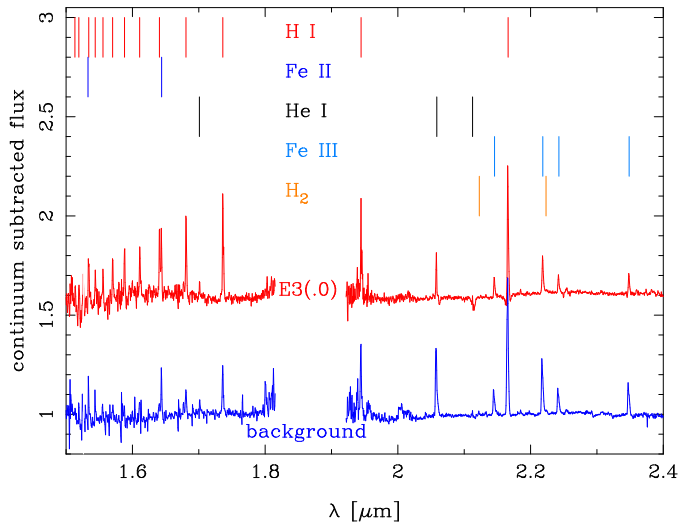
Fig. 3.— H+K-band spectrum (red) of the brightest component of IRS13E3: E3.0. For comparison the spectrum of the nebular background is shown, too (blue, shifted). In the upper part, the line positions for various transitions are marked. The weak CO band heads in the background spectrum are caused by stray light of late-type stars.

hidden in E3.0. Also, E3.0 does not resemble a dusty WR-star (of which E4.0 is one), in which case the lines would be diluted but still visible.

It is worth noting that also the background emission is well determined from our data. The seeing halo of E3.0 is of no concern since the lines in the background are stronger in relative terms. The extinction appears to be similar in the whole region, since we do not measure any change in the relative line strengths for lines from one ionization state of an element over the spectral cube. In contrast, the line strength ratios of different elements differ between the background and E3.0 (see for example the HI, FeII pseudo doublet at $1.64\,\mu m$ in Figure 3). These spatial changes in the spectral properties appear to be gradual, consistent with a gaseous nature of E3.0. They are strongest at the position of E3.0, but they do not correlate in general with the positions of the red sources in IRS13E.

The radial velocity of E3.0 determined from the Brackett-γ line is $v_{\rm LSR} \approx -25\,{\rm km/s}$, measured at the position of the continuum peak of E3.0. Paumard et al. (2006) measured a velocity of $v_{\rm LSR} = 87 \pm 20\,{\rm km/s}$ for E3 but did not identify the type of star. Probably Paumard et al. (2006) measured an average of E2 and E4.0 instead of the E3 velocity.

Given the photometric variability of E3.0, we fit the SED based on the narrow-band data set from 2004 and the one based on the SINFONI spectroscopy from 2009 separately. Using the latter we obtain $A_{\rm Ks} = 3.89 \pm 0.16$ and a warm dust component of $T = 970 \pm 17$ K, see table 2 and figure 4. The 1σ flux limit on the stellar component is $m_{\rm Ks} = 16$. Using the earlier imaging data yields consistent results. Also in this case, no stellar component is needed, however the limit is less constraining due to the smaller wavelength coverage. The extinction value $A_{\rm Ks} = 3.5 \pm 0.7$ is consistent with the former one. We also obtain an independent extinction estimate of $A_{\rm Ks} = 3.44 \pm 0.15$ from the Brackett series of E3.0

by using the relative line strengths of Hummer & Storey (1987) and the electron densities and temperatures from Lutz et al. (1993). Our different extinction estimates appear to be sufficiently consistent with each other. Using a value around $A_{\rm Ks} = 3.4$ in conjunction with the 2009 data yields that the magnitude of a possible stellar component is less than $m_{\rm Ks} = 18$.

We also compare the spectrum of E3.0 with those of young stellar objects (YSO). Such objects are not expected to reside in the central parsec, because the gas density there is much too low for star formation (Christopher et al. 2005; Bonnell & Rice 2008). Eckart et al. (2004) and Mužić et al. (2008) speculate that some of the objects in or close to IRS13E nevertheless could be YSO, arguing that shocks could allow star formation to take place. The combination of color and luminosity for E3.0 argue against a typical Herbig-B-star. Also, no distinctive feature of a massive YSO (Bik et al. 2006) is visible in E3.0. Except for the Brackett lines, the lines observed in E3.0 are unknown (e.g. FeIII) or weak (e.g. He) in massive YSO. A massive YSO does not necessarily show other lines apart from Brackett-γ in the K-band, but often CO-band heads, H_2, or the Pfund series in emission can be visible (Bik et al. 2006; Martín-Hernández et al. 2008). Such a clear indication for a YSO is not observed in E3.0, nor in other parts of IRS13E. Furthermore, there is no additional local extinction towards E3.0 while YSOs show locally enhanced extinction. We conclude that it is unlikely that E3.0 is a YSO.

The source E3.0 in the H-band has a velocity similar to the the radio source in IRS13E (Zhao et al. 2009). Therefore the H-band emission is likely due to dust associated with the gas, which causes the radio continuum emission. Hence, also qualitatively a higher extinction value (like for example expected in YSO) seems not to be needed.

Maillard et al. (2004) found two similarly bright components E3A and E3B, which is different from our result at higher resolution. Their additional stellar components do not fit our SED for E3.0. Our flux at $1.48\,\mu m$ is a factor ≈ 1.8 lower than the sum of the flux models for E3A and E3B, but at $2.18\,\mu m$ our flux is only a factor ≈ 1.15 lower. The hint for the stellar component in Maillard et al. (2004) is only based on the $1.6\,\mu m$-flux measured in the filter F160W from NICMOS. Since this is a very broad filter, and E3.0 is a very red source, the central wavelength of the filter is considerably bluer than the effective wavelength. Hence, using the central wavelength will overestimate the flux. We speculate that this effect made the stellar component necessary. Also, the amount of stellar flux contributing at that wavelength to the total flux is small, and hence a small measurement error might change the conclusion from Maillard et al. (2004).

To summarize; the potential stellar component in E3.0 is fainter than most known WR-stars. A main sequence star in E3.0 would need to be fainter than B1.5V. This seems unlikely, however, since these stars do not produce dust. With three different methods we obtained consistent extinction values, similar to the extinction towards E1 and E2. We conclude that E3.0 is neither a star nor a YSO, but rather a concentration of warm dust and gas.
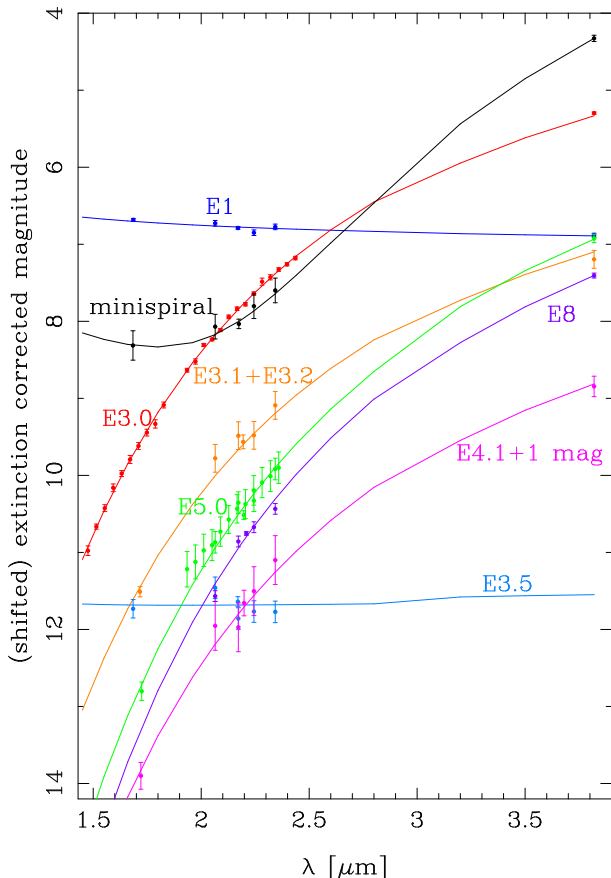
The source E3.0 is not the only dust source of its

Fig. 4.— SED data and model fits for E1, E3.0, E3.5, E4.1, E5.0, E8, the minispiral and the sum of E3.1 and E3.2. All data and fits are offset from each other for clarity. For all sources the extinction correction of E1 is applied. E1 and E3.5 are fit well by single blackbodies of stellar temperature. The objects E3.0, E3.2+E3.3, E4.1, E5.0 and E8 can be fit as single blackbodies with a dust-like temperature. Stellar components do not improve these fits. The SED of the minispiral shows two blackbodies: A warm dust component and stellar stray light.

brightness in the GC. For example, the source IRS2L resembles E3.0 in many respects and also shows extended H-band emission.

4.2.2. *E7, E8 and the surrounding gas*

The background around IRS13E is not only visible in gaseous emission lines (figure 3) but also in the continuum. The deconvolution artifacts hamper any photometric measurement of this continuum. Instead, we use the objects E7 and E8 (figure 1) that are less affected. These objects are farther away from the center of IRS13E than the other sources and likely do not belong to IRS13E but to the background. Spectroscopically, E8 appears to be indeed a local overdensity in the gas.

E7 and E8 are not detected in the H-band. We fit a blackbody model to each of the two objects, fixing the extinction to its upper bound at $A_{\rm Ks} = 3.9$. We find that no star is needed to explain the SED of these two objects. We obtain a temperature of $T = 692 \pm 55\,{\rm K}$ for E7 and of $T = 732 \pm 10\,{\rm K}$ for E8. Thus, E7 and E8 are colder than most objects in IRS13E.

We also detect three faint stars ($m_{\rm Ks} \approx 15$) in the SINFONI data at the approximately same distance ($\approx$ 450 mas) to E3.0. All these stars show CO band heads.

Buchholz et al. (2009) correctly identify the star with the strongest CO-band heads as late-type, the others are misidentified as early-type stars. The radial velocities of these stars are different from the radial velocity of IRS13E. Thus, the stars differ from IRS13E not only in proper motion (Trippe et al. 2008) but also in stellar type and radial velocity. We conclude that they are fore- or background objects.

The background around IRS13E is part of the minispiral (Lo & Claussen 1983; Paumard et al. 2004; Zhao et al. 2009). The minispiral is visible in our L'- and Ks-band data. In order to measure its SED, we select seven boxes of ≈ 0.2" diameter far away from bright stars at a distance of around 1.5" to IRS13E. We exclude the narrow-band data around Brackett-γ because of the strong emission line there. We calibrate the flux from the narrow-band filters in absolute terms by fitting these flux values as a linear function of wavelength and setting equal the flux at $2.18\,\mu$m to the measured Ks-band flux. We fit two blackbodies to the SED data (Figure 4). One accounts for the stellar stray light, the other represents the dust. The fits for all fields are similar. The average extinction is $A_{\rm Ks} = 3.64 \pm 0.55 \pm 0.56$, consistent with the extinction value derived for E1. The average dust temperature is $T = 585 \pm 22 \pm 33\,{\rm K}$. Thus, the minispiral is colder than the dust in IRS13E.

One of the seven fields contains the central sources of IRS13N (Eckart et al. 2004; Moultaka et al. 2005; Mužić et al. 2008). In this case the fit yields $A_{\rm Ks} = 3.7 \pm 1.6$ and $T = 664 \pm 174\,{\rm K}$. This argues against a highly extincted object (like a YSO) as these authors had proposed. The object IRS13Nβ is within the field of view of our SINFONI data. We do not find any significant differences between its spectrum and the spectrum of the gas around IRS13E. Also, the velocity of IRS13N in L'-band (Mužić et al. 2008) and at radio wavelengths (Zhao et al. 2009) make it more likely that IRS13N actually consists of dust blobs. They appear denser than in other regions in the GC, but still they are much less prominent than E3.0. The common proper motion of these sources (Mužić et al. 2008) could also be explained by a recent formation of the dust clouds.

5. PROBABILITY FOR AN IMBH IN IRS13E

We now discuss the nature of IRS13E considering our NIR observations. There are four main explanations:

- IRS13E is a cluster in the process of dissolution (Schödel et al. 2005). This is very unlikely, because it would get diluted extremely quickly. We estimate that after just 200 years one would not recognize anymore the overdensity of three young, massive stars as such. We exclude this option.

- IRS13E is a cluster bound by stellar mass. From our detection limits, we estimate that the total stellar mass of the cluster could at most be 2000 $M_{\odot}$.

- IRS13E is a cluster bound by additional mass, e.g. an IMBH.

- IRS13E is a chance association.

5.1. *Stellar surface density in IRS13E*

Name	data	spectral type	A_{Ks}	T_1 [K]	T_2 [K]	star $m_{1,\,\mathrm{Ks}}$	dust $m_{2,\,\mathrm{Ks}}$
E1	NB, H, K, L	OB I	3.64 ± 0.07	27500		10.38 ± 0.06	
E2	SINF, NB, H, K, L	WN 8	3.51	30000	712	10.43	14.74
E3.0	SINF, NB, H, K, L	gas	3.89 ± 0.16	9480	970 ± 17	> 16	11.42 ± 0.05
E3.1+E3.2	NB, H, K, L	gas	3.9	9480	955 ± 24	> 18.03	13.24 ± 0.18
E3.3	NB, H, K, L	gas	3.9	9480	987 ± 54	> 15.16	13.65 ± 0.35
E3.4	NB, H, K, L	gas	3.9	9480	954 ± 49	> 16.53	14.15 ± 0.36
E3.5	NB, H, K		3.49 ± 0.36	4000-19000		15.30 ± 0.26	
E4.0	SINF, NB, H, K, L	WC 9	3.64	41000	1400	11.95	12.51
E4.1	NB, H, K, L	gas	3.9	9480	844 ± 24	> 18.36	14.38 ± 0.21
E4.2	NB, K, H		3.9	4000-19000	517 ± 252	15.77 ± 0.11	16.64 ± 2.5
E4.3	K						15.48 ± 0.10
E5.0	SINF, NB, H, K, L	gas	3.4	9480	700 ± 8	> 18.46	14.08 ± 0.10
E5.1	NB, H, K, L	gas	3.9	9480	947 ± 25	> 17.75	14.25 ± 0.14
E5.2	NB, K, L	gas	3.9	9480	642 ± 70	> 15.6	15.49 ± 0.10
E5.3	NB, H, K	gas	3.9	9480	978 ± 524	> 16.04	15.1 ± 1.6
E5.4	NB, K	gas	3.4		817 ± 474		15.54 ± 2
E6	NB, H	K3III	3.68 ± 0.09	4300		13.82 ± 0.10	
E7	NB, K, L		3.9	9480	692 ± 55	> 16.71	16.02 ± 0.40
E8	NB, K, L	gas	3.9	9480	732 ± 10	> 17.14	14.51 ± 0.11

NOTE. — We fit one or two blackbodies with temperatures T_1 and T_2 and one extinction parameter to our SED data. We allow extinction values between $A_{\mathrm{Ks}} = 3.4$ and $A_{\mathrm{Ks}} = 3.9$ and clip it if needed at the respective edge of the interval. We derive the temperature of the stellar component from an atmosphere model or from the observed lines when possible. Otherwise the temperature is set to $T = 9480$ K. All limits are 1σ-limits. In column two, SINF means the SED fitting results are based on SINFONI data, NB that the narrow band images are used.

A physical cluster leads to an overdensity in projection compared to the local background density. Detecting a local, significant overdensity in the stellar surface density would hence be a strong indication that IRS13E is a cluster. From our data we measure the projected space densities of stars in IRS13E. Paumard et al. (2006) found 13 objects with $m_{\mathrm{H}} < 19.4$ inside a radius of 0.3" in IRS13E. Similarly, we find 15 objects in H- and Ks-band with $m_{\mathrm{H}} < 18.5$ inside a radius of $0.27''$.

We determine the density of background stars in a non-confused region north of IRS13E for stars fainter than $m_{\mathrm{H}} = 14$ and use the results from Genzel et al. (2003) for brighter stars. We find that the density of objects in IRS13E is higher than in the surrounding field at nearly all magnitudes (figure 5), if all objects are considered. However, only for six of these objects a star is required to explain the observed SED. For the other objects, a possible stellar component needs to be fainter than about $m_{\mathrm{Ks}} \approx 15.5$. This corresponds to a stellar surface density of $26\,\mathrm{as}^{-2}$, which is five times higher than the background. However, E6 is not a member of the cluster, given its age well above 6 Myr. Furthermore, the two faint stars E3.5 and E4.2 have magnitudes consistent with the red clump and hence are likely also older than the bright stars. In the magnitude bin of E3.5 and E4.2, the background population accounts already for one of the two stars. Thus, the overdensity in this bin is insignificant, too.

We conclude that the magnitude integrated overdensity of IRS13E (chance probability of 2×10^{-5} according to Paumard et al. (2006)) is caused by dust clumps and not by stars. This overdensity cannot be used as evidence for a cluster. We analyze the significance of the concentration of the three bright early-type stars in IRS13E in section 5.3.
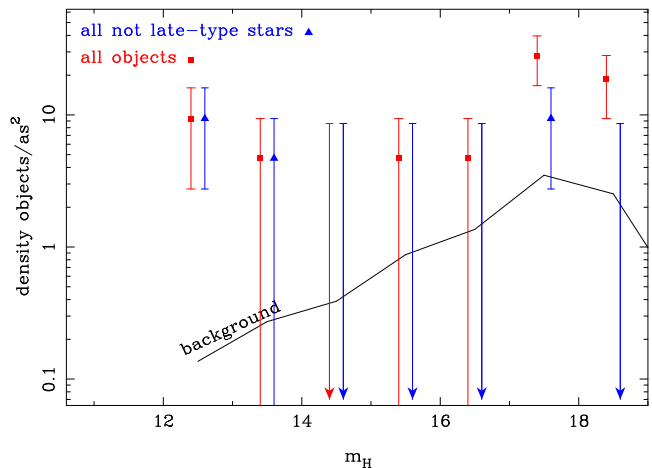
5.2. The structure of IRS13E

Fig. 5.— Surface densities of objects in the core ($r = 0.27$") of IRS13E. The errors are Poisson errors. The upper limits are 1σ-limits. Red: All objects. Blue: Cluster member candidates only. The red data are shifted for clarity by 0.1 mag to the left, the blue by the same amount to the right. The solid line shows the estimated background density for our data.

In the H-band the dust blobs in IRS13E are brighter than all other non-stellar structures in the central parsec, except the ones which are related directly to a star. They are nearly twice as hot as the minispiral and also denser ($\approx 4\times$ for E3.0, estimated from surface brightness and temperature) than the minispiral. The brightest and hottest dust blobs (around E3.0) are located between the two bright WR-stars E2 and E4.0. The star E2 is the brightest of all WR stars in the GC and E4.0 is a dusty WR with the hottest dust in IRS13E.

Therefore E4.0 might be the most important dust source in IRS13E. But it seems unlikely that E4.0 is responsible alone for the bright dust blob E3.0, given that it does not move away from E4.0, while the motions of the blobs E4.1 and E4.3 are consistent with being out-
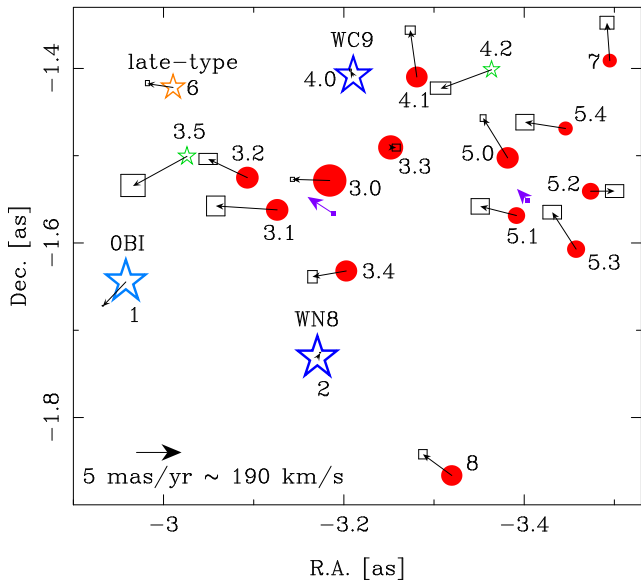
FIG. 6.— Velocities of the objects in IRS13E relative to the mean motion of the two WR-stars E2 and E4.0. The near-infrared motion are marked with black arrows with boxes as 1-σ errors. Stars are marked with asterisks (blue: young stars; green: stars without spectral identification). Dust clumps are marked by red disks. The sizes of symbols indicate the Ks-band flux. The 13 mm radio motions (violet) of Zhao et al. (2009) are shown, too.
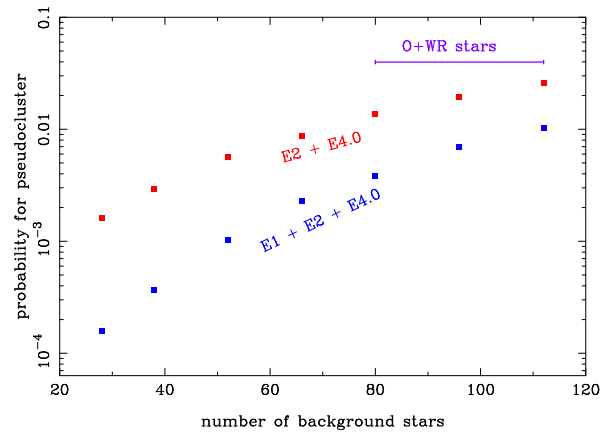

FIG. 7.— Probability for observing a cluster of two or three early-type stars that resemble IRS13E in a background population of given sample size. The violet bar marks the range applicable for the GC.

flows from E4.0. Instead, we assume that the winds of E2 and E4.0 collide in the E3 region and cause the bright dust blobs in this way. The fact that the velocities of these blobs are not pointing towards either of the two WR stars supports this picture. Also, the R.A. motion of the more eastern blobs is smaller than of the western blobs as expected in this model. Accordingly, E2 and E4.0 would not only be close in projection, but also in the line of sight.

A potential weakness of that model is that the motions of the blobs E3.3 and E4.1 do not immediately fit. But this is only a worry if no other forces act on the winds. For example, the presence of the gas from the minispiral might decelerate the winds. A second problem might be that it is not clear whether the conditions for dust formation are satisfied, given that our system is very different from WR140 (Monnier et al. 2002).

Most likely E1 does not contribute to the dust production. It is further away and supergiants have weaker winds than WR-stars. Furthermore, the velocities of some dust clumps are pointing towards E1. Therefore E1 can, but needs not to be close in real space to the WR-stars.

The dust clumps in E5, E7 and E8 fit less well into our simple model of two WR stars because of their velocities. They are also mostly colder than the dust clumps in E3 and E4, but still warmer than the minispiral. In addition, they are farther away from E2 and E4.0. Likely the minispiral is more important for their formation.

5.3. The overdensity of young, massive, early-type stars

Because most of the fainter objects in IRS13E are dust clumps, the most prominent feature of the potential cluster IRS13E is the concentration of the three bright stars. Their density is ≈ 30 times higher in IRS13E compared to the local background. Therefore we quantitatively

evaluate the argument of Maillard et al. (2004), that this association cannot be a chance occurrence. On the one side, the number of stars is very small, and one could argue that IRS13E cannot be a significant overdensity. On the other hand, five or even six phase space coordinates of these stars are similar.

We calculate the probability that a star association like IRS13E occurs randomly, i.e. a pseudocluster, by means of Monte Carlo simulations. IRS13E cannot be part of the clockwise disk of young stars (Paumard et al. 2006). Consequently, the size of the sample of stars considered is chosen to equal the observed population of those O- and WR-stars that are not part of the clockwise disk, which yields 96 stars with $r < 10''$. We assume that as many of the counterclockwise moving stars are in a disk-like configuration as suggested by Bartko et al. (2009); the rest is on randomly oriented orbits. The disk thickness and eccentricity distribution are chosen to match the observed ones of the well-defined, clockwise disk. The distribution of semi-major axes is chosen such that the final surface density profile resembles the observed one. The actual number of stars is varied, too. On purpose, we don't restrict the sample to the stars at least as bright as the IRS13E members. Fainter O-stars are barely less massive, and dynamically they would not behave any differently (Portegies Zwart et al. 2007).

By randomly drawing a stellar distribution many times with the given assumptions, we find that a triple of stars similar to E1, E2 and E4.0 has a chance probability of 0.7%, and that finding a pair of stars that matches E2 and E4.0 has a chance probability of 1.9%, see figure 7. Demanding in addition that E2 and E4.0 have similar masses lowers the chance probability for such a pair to 0.1%, since only 28 of the 96 stars from which we draw the pseudoclusters have masses comparable to that of E2 and E4.0. Hence, the occurrence of a pseudocluster similar to IRS13E is not expected, but still not impossible.

We also note that E2 and E4.0 could form a binary in a distant orbit around the central parsec. Heavy binaries indeed often consist of two similarly massive stars (Kobulnicky & Fryer 2007).

5.4. Cluster mass from velocity dispersion

Because the probability for IRS13E being a chance association is relatively small, it is reasonable to exploit the idea that IRS13E indeed is a cluster. Therefore we estimate the mass needed to bind the cluster by analyzing the velocity dispersion.

5.4.1. *Assuming E1, E2 & E4.0 are cluster members*

Classical mass estimators are very uncertain when applied to a sample of three stars only. Hence, we simulate clusters of three stars around a central mass in a Monte Carlo fashion for deriving the probability distribution for the value of the mass. For this one needs to marginalize over many parameters, mainly the 18 orbital elements of the three stars.

We assume that all angles and phases are randomly distributed and that the eccentricities follow a thermal distribution $n(e) \propto e$. The semi-major axes a are drawn from $a = 0.4'' \times p^{0.9}$, where p is a random number in [0,1]. This makes the distribution of projected distances similar to the observed one. In this way we simulate 5×10^8 clusters around different IMBH with masses between $300\,M_\odot$ and $3 \times 10^5\,M_\odot$ in steps of $\Delta M/M = 0.15$.

The peculiar property of IRS13E is that one star has a significantly different velocity compared to the other two. Thus, we choose from the simulated clusters the ones, which have nearly the same velocity differences as the observed cluster. We neglect the exact spatial distribution of the stars in IRS13E, but on average the simulated stars from the chosen clusters are at similar positions as the observed stars. Since we assume here that IRS13E is a cluster, we normalize the probability such that the total probability of clusters accepted over the full mass range is 1.

We derive that the mass in this case is $M_{\mathrm{IMBH}} = 13900^{+34300}_{-10800}\,M_\odot$. The probability distribution for M_{IMBH} is highly non-Gaussian, see black curve in Figure 9. The large mass error is due to the low number of stars. Nevertheless, the mass needed to bind IRS13E exceeds the mass of the three stars. Hence, if IRS13E is a cluster of three stars, it likely also hosts an IMBH.

5.4.2. *Assuming only E2 & E4.0 are cluster members*

If one assumes that E2 and E4.0 form an equal-mass binary, the measured velocity difference yields a mass for each star of $180\,M_\odot$. Consequently, an IMBH with a mass of similar size suffices to bind the two stars, too. Since that binding mass is less than the limit on the stellar mass in IRS13E ($2000\,M_\odot$), one would not need an IMBH to explain IRS13E.

The simple binary hypothesis is problematic. The tidal forces of the SMBH disrupt a binary with a separation larger than the Hill-radius (Binney & Tremaine 2008) during pericenter passage. For a bound, equal mass binary there exists no value of the unknown line-of-sight distance $|z|$ that would make the binary survive a pericenter passage (figure 10). Also, the destruction timescale for such a soft binary in a distance of 6" to the SMBH is only 27000 years (calculated for the observed projected separation of E2 and E4.0, Binney & Tremaine (2008)). Furthermore, a mass of $180\,M_\odot$ per star seems unrealistic. These arguments make the binary hypothesis less likely than assuming that additional mass is needed for binding E2 and E4.0. Still, the mass needed would
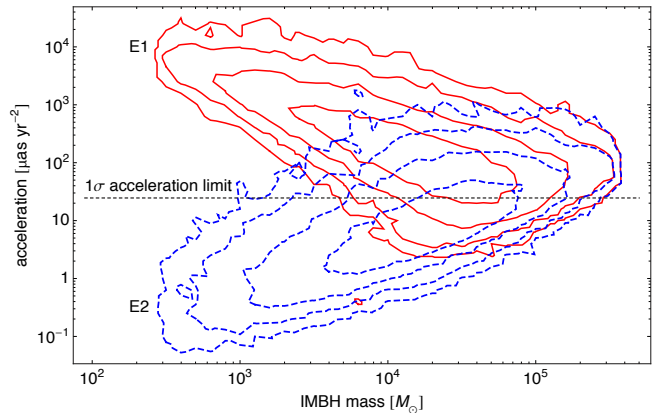

FIG. 8.— Contour plot of the distributions of plane of sky accelerations for the simulated stars in our Monte Carlo clusters. The contour lines are drawn at the position where in any given logarithmic bin of size (0.1, 0.2) respectively 10, 30, 100, 300 or 1000 of the simulated 50000 clusters are found. Solid lines: simulations for E1, dashed lines: simulations for E2. The horizontal line represents our acceleration limit. The region above the line is excluded at the 1σ-level.

not imply an IMBH. Finally, the mass estimate could be too high due to the measurement errors. A mass per star of $85\,M_\odot$ is excluded only at the 2σ-level.

5.5. *Mass limits from acceleration limits*

An IMBH can manifest itself in the accelerations it imposes on surrounding stars. Vice versa, the absence of accelerations places limits on the mass of an potential IMBH. From our data we can only test for accelerations in the proper motions:

$$a_{\mathrm{2D}} = \frac{r_{\mathrm{2D}}}{R_{\mathrm{3D}}} \cdot \frac{G\,M_{\mathrm{IMBH}}}{R_{\mathrm{3D}}^2} = G\,M_{\mathrm{IMBH}}\,\frac{r_{\mathrm{2D}}}{(r_{\mathrm{2D}}^2 + z^2)^{3/2}} \quad (1)$$

We do not measure any significant accelerations (table 1). Firstly, this sets only limits on the location of the stars relative to the IMBH along the line of sight (z). But secondly, it is unlikely that a cluster extends much more in the z-dimension than in the plane of sky, and this actually constrains the mass M_{IMBH} of the IMBH.

We adopt again a Monte Carlo approach, using the same simulations as in section 5.4. For all simulated clusters, we calculate the expected values of a_{2D}.

Figure 8 shows that the star E1 is most constraining. This is due to the fact that its velocity differs from the one of E2 and E4.0. Hence, it is more likely that the IMBH is located closer to E1 than to the other two stars, which in turn means that its motion is more sensitive to the mass of the IMBH. The simulated data for E4.0 are similar to the one for E2, but the measurement errors of E4.0 are four times as big. As consequence, only the acceleration limit of E1 is important.

Figure 8 shows that E1 excludes an IMBH of lower mass more efficiently than an IMBH of higher mass. This seems paradoxical, but results from the fact that the lower the mass is, the more likely it is that the IMBH resides close to E1. If the IMBH is close to E1, the full velocity difference between E1 and the other stars is due to E1 and one can write.

$$\frac{m_{\mathrm{E1}}(\delta v)^2}{r_{\mathrm{E1}}} = \frac{G\,M_{\mathrm{IMBH}}\,m_{\mathrm{E1}}}{r_{\mathrm{E1}}^2} \rightarrow r_{\mathrm{E1}} = \frac{M_{\mathrm{IMBH}}}{(\delta v)^2} \quad (2)$$
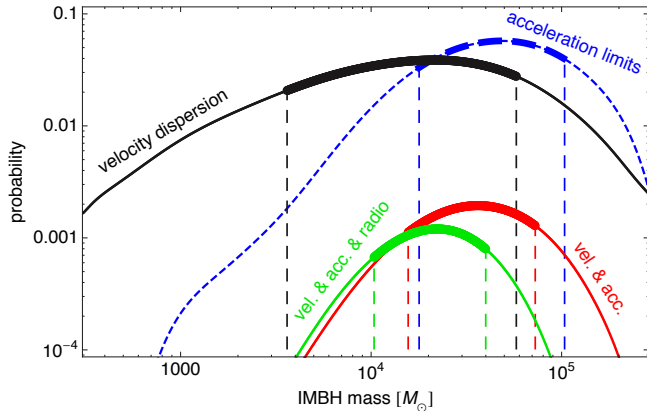
FIG. 9.— Probabilities for different IMBH masses, if IRS13E is a gravitationally bound star cluster of 3 stars (E1,E2, E4.0). The blue, dashed curve gives the probability to observe the measured acceleration limits for an assumed mass of the IMBH. Black: Probability distribution of the mass of the IMBH from the measured velocity differences, assuming that an IMBH is present; hence the integral over this distribution equals 1. Red: Combining velocity and acceleration information, yielding a total probability of 2.8%. Green: Using in addition the limit of the radio motion of Sgr A* from Reid & Brunthaler (2004). The integral over the distribution now is only 1.5%. The thick regions mark the respective 1σ intervals of the most likely masses.

Reducing M_{IMBH} thus lowers r_{E1} if the velocity difference has to stay at the measured value. For the acceleration a_{E1} follows

$$a_{\mathrm{E1}} \propto \frac{M_{\mathrm{IMBH}}}{r_{\mathrm{E1}}^2} \propto \frac{(\delta v)^4}{M_{\mathrm{IMBH}}} \qquad (3)$$

This anti-proportionality of acceleration to M_{IMBH} is visible in the simulations (red, solid contours in figure 8).

For obtaining a probability distribution of M_{IMBH} we compare in mass bins the probability for the simulated clusters with the probability to observe the measured acceleration limits if $M_{\mathrm{IMBH}} = 0$ (figure 9). An IMBH with $M_{\mathrm{IMBH}} < 10000\,M_\odot$ has a probability of less than 1.5%. At the most probable mass of $14000\,M_\odot$ the fact that no acceleration was detected yields a probability of 2.5%. For all mass bins the probability of $M_{\mathrm{IMBH}} > 0$ is less than 8%.

The mass estimate of $\approx 1000\,M_\odot$ from the assumption that only E2 and E4 are bound would yield an acceleration of $\approx 3\,\mu\mathrm{as/yr}^2$. This is smaller than our measurement accuracy and we cannot test the hypothesis.

5.6. Total probability

The combined probability for not detecting an acceleration under the assumption that E1, E2 and E4.0 form a cluster, bound by an IMBH, is the product of the probability distribution for the mass given the observed velocity dispersion with the probabilities for not detecting accelerations (figure 9). The integrated probability (i.e. asking what is the probability for the presence of an IMBH) is then lowered to 2.8%. As expected, the acceleration limits reduce the probabilities at all masses. The most likely mass of an IMBH is shifted to $40000\,M_\odot$ and masses below $5000\,M_\odot$ are excluded. This means, if IRS13E is cluster of three stars, an IMBH is present.

6. DISCUSSION

We are left with a puzzle. It is unlikely that the three stars are a pseudocluster, given that the chance of finding an overdensity like IRS13E has a probability of 0.7%. On the other hand, given our acceleration limits, the presence of an IMBH has a small probability of 2.8%, too. Both explanations seem unlikely at a similar level. We therefore consider additional arguments.

6.1. Proper motion of Sgr A*

Gualandris & Merritt (2009) show that the proper motion of Sgr A* perpendicular to the plane of the Galaxy (Reid & Brunthaler 2004) is the most promising method for excluding an IMBH at distances similar to that of IRS13E. For IRS13E itself, we can take advantage of the fact that we know the velocity of the potential cluster and hence of the proposed IMBH. We can predict the expected reflex motion of Sgr A* and do not need to assume circular motion in the plane of sky, as Gualandris & Merritt (2009) had to.

Hence, we calculate for all mass bins the probability for measuring the observed motion of Sgr A*. We use the value from Reid & Brunthaler (2004) who find that the motion perpendicular to the Galactic plane is $-0.4 \pm 0.9\,\mathrm{km/s}$. We estimate the uncertainty of the motion of the IMBH simply by the velocity dispersion of the potential cluster. We fold the result into the arguments of section 5.6 (figure 9). The small negative proper motion of Sgr A* actually raises the probability for a small IMBH slightly. But very massive IMBH are excluded efficiently. From the combined analysis the most probable mass of an IMBH for three stars is $20000\,M_\odot$, and the total probability (integrated over all masses) for the presence of an IMBH is lowered to 1.5%.

6.2. Dynamics of the young, massive stars

The clockwise disk of early-type stars in the GC is significantly warped (Bartko et al. 2009). Such a warp can be the consequence of another non-spherical mass (Nayakshin 2005; Löckmann & Baumgardt 2009), and thus an IMBH might manifest itself via the warp. However, there are many other possibilities to explain the warp: The counterclockwise disk might suffice, or the warp can also happen in the gaseous phase during the disk formation (Hobbs & Nayakshin 2009). Dynamical friction will make an IMBH spiral down to the SMBH (Fujii et al. 2009), such that it would stay only for a very short time in the radial region of the disks. Hence, an IMBH is a less efficient warper per mass than a disk.

One possible origin of a potential IMBH is the core collapse of a young, massive star cluster (Portegies Zwart & McMillan 2002). IRS13E could be the remainder of such an object that currently is spiraling in. This scenario is disfavored as origin for the young, massive stars (Paumard et al. 2006; Bartko et al. 2009; Bartko et al. 2010). Here, we make the argument that the number of young, massive stars in the GC does not match what one would expect for the most likely mass of an IMBH of $20000\,M_\odot$.

It turns out that there are too few massive stars in the GC outside IRS13E for this scenario. In the simulations of Portegies Zwart & McMillan (2002); Portegies Zwart et al. (2004); Fujii et al. (2009) the IMBH obtains a mass of 0.1% to 9% of the total initial mass of the cluster, depending on the assumptions
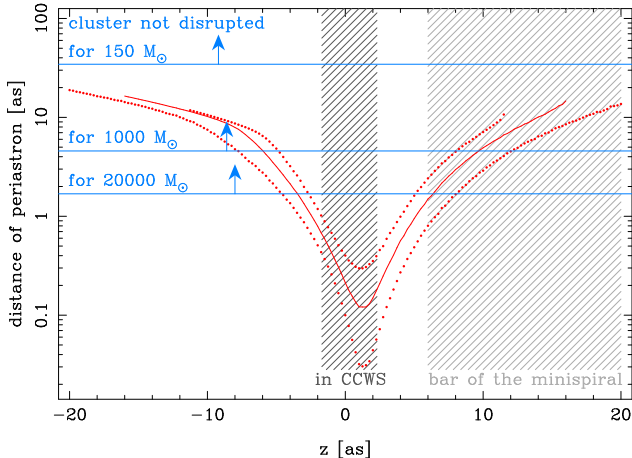
FIG. 10.— Periastron distance of IRS13E for possible locations along the line of sight (z) in the point mass potential of the SMBH. The dotted lines mark the 1σ-error band. Considering tidal disruption, only the z positions corresponding to periastron distances above the blue lines are possible for the respective masses. The two lower lines for 1000 and 20000 $M_\odot$ assume a cluster with an IMBH, the upper line is for the case that E2 and E4.0 form a binary with 150 $M_\odot$ per star. The shaded region close to $z = 0''$ corresponds to the cases in which IRS13E is in the counterclockwise disk (CCWS) (Bartko et al. 2009). The shaded region to the right corresponds to a location of IRS13E in the minispiral (Paumard et al. 2004), which is possible for all configurations. It is not possible, that an IMBH binds IRS13E, and that at the same time IRS13E is located in counterclockwise disk.

on the IMF, the radii and winds of very massive stars, the density of the cluster and whether a single supernova stops the formation of the IMBH. Thus, for the most likely IMBH mass one needs an initial cluster mass of at least $2 \times 10^5 \, M_\odot$ (Fujii et al. 2009). Assuming a Salpeter IMF between 1 and 140 $M_\odot$ (Fujii et al. 2009), stars more massive than 40 $M_\odot$ would merge into the IMBH. The lighter stars should still be observable today, and one would expect to find 790 O-stars $(20 - 40 \, M_\odot)$ and 1950 early B-stars $(10 - 20 \, M_\odot)$.

In the GC there are in total only ≈ 290 O/WR-stars, correcting the currently detected number of such stars upward by a factor of 2.4, as estimated from incomplete areal coverage and detection incompleteness (Figure 2 in Bartko et al. (2010)). However, not all of them are compatible with the idea that they originate from IRS13E.

Figure 10 shows that it is not possible that an IMBH binds IRS13E, and that at the same time IRS13E is located in the counterclockwise disk. Hence, the inspiraling cluster scenario requires that the orbits of the stars stripped off the cluster are found in edge-on orbits in a common orbital plane. We estimate that at most 50 O/WR-stars could have such orbits. We observe however a factor 15 fewer O-stars. For the bright B-stars, the discrepancy is even larger. We conclude that the formation of an IMBH of 20000 $M_\odot$ in IRS13E is inconsistent with the observed number of young stars.

6.3. X-ray and radio emission

Apart from Sgr A*, IRS13E is the only region in the GC which is bright in the NIR, at radio wavelengths (Zhao & Goss 1998) and in X-rays (Wang et al. 2006). At 13 mm, the morphology of the minispiral is similar to the one in L'-band. This emission traces colliding gas, probably associated with the dust visible in the NIR.

The X-ray spectrum of IRS13E (Wang et al. 2006) is similar to the diffuse X-ray emission from the local background and from the region around Sgr A*. Coker et al. (2002) argue, that IRS13E is a wind nebula excited by a star, which left the Luminous Blue Variable (LBV) phase a short time ago. Maybe this scenario also works for the two WR-stars the winds of which probably collide in E3. The accuracy of the position of the X-ray source is not sufficient to decide whether the X-ray source can be identified with any of the bright NIR sources in IRS13E.

The observed flux in IRS13E is $L_{\rm X}(2 - 10 \, {\rm keV}) = 2 \times 10^{33} \, {\rm erg/s}$ (Wang et al. 2006), corresponding to $\approx 10^{-9}$ Eddington luminosities ($L_{\rm Edd}$) for an IMBH of 20000 $M_\odot$. This number is much smaller than for the X-ray binaries detected in the GC (Muno et al. 2005). However, Sgr A* itself is radiating in quiescence with only $L_{\rm X}(2 - 10 \, {\rm keV}) = 4 \times 10^{-12} L_{\rm Edd}$ (Baganoff et al. 2001) such that a low radiative efficiency does not exclude the presence of an IMBH right away. A comparison on basis of the X-ray flux only is difficult, since the environment and accretion state might differ significantly between Sgr A* and an IMBH in IRS13E.

There is no variability reported for IRS13E in the X-rays (Muno et al. 2005), despite the fact that during roughly half of the observations of Sgr A* IRS13E was observed, too. Many black holes are variable in the X-ray domain (examples are X-ray binaries (Muno et al. 2005) and Sgr A* (Baganoff et al. 2001; Porquet et al. 2003)). In section 5.2 we argue that the dust seen in IRS13E is physically connected with the group of stars. Comparing the Br-γ emission in IRS13E and close to Sgr A* shows that the gas reservoir in the IRS13E is much richer than close to the SMBH. Taken together, this makes it unlikely that the reported, steady source is due to an IMBH.

7. CONCLUSIONS AND SUMMARY

We present a detailed analysis of the potential cluster IRS13E in the GC. We use AO-based images in H- and Ks-band from 2002 to 2009 for identifying objects in IRS13E and for performing astrometry. We detect 19 objects on most high Strehl ratio images in Ks-band and 15 of them also in H-band. The proper motions of the objects are well determined.

In addition, we characterize the SED of the objects in IRS13E using AO-based integral field spectroscopy (1.45 to 2.45 μm) for the brighter objects and (narrow-band) imaging from H- (1.66 μm) to L'-band (3.80 μm) for the fainter objects. We fit the SED of the objects by a model consisting of two blackbodies and an extinction parameter. From this we conclude that 13 objects are dust clumps without embedded stars and that the extinction appears to be constant in the IRS13E region. Three objects are fainter stars: One is a spectroscopically identified late-type star. The two fainter stars of the magnitude of the red clump are consistent with the expected number of stars per area at this magnitude bin. Thus, these three stars are likely background stars. Therefore, IRS13E is only a concentration of the remaining three early-type stars E1, E2 and E4.0.

They have the following properties:

- E2 and E4.0 are located close in 3D, because of the bright dust clumps between them.

- A chance association of three early-type stars has

a probability of only 0.7%.

- If one assumes the existence of a binding mass, we derive a mass of around 20000 $M_\odot$ from a combination of the velocities of the stars, acceleration limits and the fact that Sgr A* appears to be at rest. This mass exceeds the stellar mass (inclusive faint, invisible stars) in IRS13E.

- Our non detection of accelerations and the insignificant radio motion of Sgr A* yield only a probability

of 1.5% for an IMBH in IR13E.

- There are roughly 15 times too few young stars in the GC for the formation of an IMBH as massive as 20000 $M_\odot$.

- The weak and non-variable X-ray source in IRS13E makes the presence of an IMBH unlikely.

Overall, we conclude that it is more likely that IRS13E does not host an IMBH.

REFERENCES

Allen, D. A., Hyland, A. R., & Hillier, D. J. 1990, MNRAS, 244, 706
Baganoff, F. K., et al. 2001, Nature, 413, 45
Bartko, H., et al. 2009, ApJ, 697, 1741
Bartko, H., et al. 2010, ApJ, 708, 834
Bik, A., Kaper, L., & Waters, L. B. F. M. 2006, A&A, 455, 561
Binney, J., & Tremaine, S. 2008, Galactic Dynamics: Second Edition (Princeton University Press)
Blum, R. D., Sellgren, K., & Depoy, D. L. 1996, ApJ, 470, 864
Bonnell, I. A., & Rice, W. K. M. 2008, Science, 321, 1060
Bonnet, H., et al. 2003, in Society of Photo-Optical Instrumentation Engineers (SPIE) Conference Series, Vol. 4839, Society of Photo-Optical Instrumentation Engineers (SPIE) Conference Series, ed. P. L. Wizinowich & D. Bonaccini, 329–343
Buchholz, R. M., Schödel, R., & Eckart, A. 2009, A&A, 499, 483
Christopher, M. H., Scoville, N. Z., Stolovy, S. R., & Yun, M. S. 2005, ApJ, 622, 346
Coker, R. F., Pittard, J. M., & Kastner, J. H. 2002, A&A, 383, 568
Crowther, P. A. 2007, ARA&A, 45, 177
Diolaiti, E., Bendinelli, O., Bonaccini, D., Close, L. M., Currie, D. G., & Parmeggiani, G. 2000, in Presented at the Society of Photo-Optical Instrumentation Engineers (SPIE) Conference, Vol. 4007, Proc. Society of Photo-Optical Instrumentation Engineer Vol. 4007, p. 879-888, Adaptive Optical Systems Technology, Peter L. Wizinowich; Ed., ed. P. L. Wizinowich, 879–888
Draine, B. T. 1989, in ESA Special Publication, Vol. 290, Infrared Spectroscopy in Astronomy, ed. E. Böhm-Vitense, 93–98
Eckart, A., Moultaka, J., Viehmann, T., Straubmeier, C., & Mouawad, N. 2004, ApJ, 602, 760
Eckart, A., Moultaka, J., Viehmann, T., Straubmeier, C., & Mouawad, N. 2004, ApJ, 602, 760
Eisenhauer, F., et al. 2003, SPIE, 4841, 1548
Forrest, W. J., Shure, M. A., Pipher, J. L., & Woodward, C. E. 1987, in American Institute of Physics Conference Series, Vol. 155, The Galactic Center, ed. D. C. Backer, 153–156
Fritz, T. K., et al. 2010, MNRAS, 401, 1177
Fujii, M., Iwasawa, M., Funato, Y., & Makino, J. 2009, ApJ, 695, 1421
Genzel, R., Thatte, N., Krabbe, A., Kroker, H., & Tacconi-Garman, L. E. 1996, ApJ, 472, 153
Genzel, R., et al. 2003, ApJ, 594, 812
Gerhard, O. 2001, ApJ, 546, L39
Ghez, A. M., et al. 2003, ApJ, 586, L127
—. 2008, ApJ, 689, 1044
Gillessen, S., Eisenhauer, F., Trippe, S., Alexander, T., Genzel, R., Martins, F., & Ott, T. 2009, ApJ, 692, 1075
Gualandris, A., & Merritt, D. 2009, ArXiv e-prints
Hansen, B. M. S., & Milosavljević, M. 2003, ApJ, 593, L77
Hillier, D. J., & Miller, D. L. 1998, ApJ, 496, 407
Hobbs, A., & Nayakshin, S. 2009, MNRAS, 394, 191
Hummer, D. G., & Storey, P. J. 1987, MNRAS, 224, 801
Kobulnicky, H. A., & Fryer, C. L. 2007, ApJ, 670, 747
Krabbe, A., Genzel, R., Drapatz, S., & Rotaciuc, V. 1991, ApJ, 382, L19

Lenzen, R., et al. 2003, in Presented at the Society of Photo-Optical Instrumentation Engineers (SPIE) Conference, Vol. 4841, Instrument Design and Performance for Optical/Infrared Ground-based Telescopes. Edited by Iye, Masanori; Moorwood, Alan F. M. Proceedings of the SPIE, Volume 4841, pp. 944-952 (2003)., ed. M. Iye & A. F. M. Moorwood, 944–952
Lo, K. Y., & Claussen, M. J. 1983, Nature, 306, 647
Löckmann, U., & Baumgardt, H. 2009, MNRAS, 394, 1841
Lu, J. R., Ghez, A. M., Hornstein, S. D., Morris, M. R., Becklin, E. E., & Matthews, K. 2009, ApJ, 690, 1463
Lucy, L. B. 1974, AJ, 79, 745
Lutz, D., Krabbe, A., & Genzel, R. 1993, ApJ, 418, 244
Lutz, D., et al. 1996, A&A, 315, L269
Maillard, J. P., Paumard, T., Stolovy, S. R., & Rigaut, F. 2004, A&A, 423, 155
Maness, H., et al. 2007, ApJ, 669, 1024
Martín-Hernández, N. L., Bik, A., Puga, E., Nürnberger, D. E. A., & Bronfman, L. 2008, A&A, 489, 229
Martins, F., Genzel, R., Hillier, D. J., Eisenhauer, F., Paumard, T., Gillessen, S., Ott, T., & Trippe, S. 2007, A&A, 468, 233
Martins, F., Hillier, D. J., Bouret, J. C., Depagne, E., Foellmi, C., Marchenko, S., & Moffat, A. F. 2009, A&A, 495, 257
Monnier, J. D., Tuthill, P. G., & Danchi, W. C. 2002, ApJ, 567, L137
Moultaka, J., Eckart, A., Schödel, R., Viehmann, T., & Najarro, F. 2005, A&A, 443, 163
Muno, M. P., Pfahl, E., Baganoff, F. K., Brandt, W. N., Ghez, A., Lu, J., & Morris, M. R. 2005, ApJ, 622, L113
Mužić, K., Schödel, R., Eckart, A., Meyer, L., & Zensus, A. 2008, A&A, 482, 173
Nayakshin, S. 2005, MNRAS, 359, 545
Nishiyama, S., Tamura, M., Hatano, H., Kato, D., Tanabé, T., Sugitani, K., & Nagata, T. 2009, ApJ, 696, 1407
Ott, T. 2002, PhD thesis, Ludwig-Maximilians-Universitaet Muenchen
Paumard, T., Maillard, J.-P., & Morris, M. 2004, A&A, 426, 81
Paumard, T., et al. 2006, ApJ, 643, 1011
Porquet, D., Predehl, P., Aschenbach, B., Grosso, N., Goldwurm, A., Goldoni, P., Warwick, R. S., & Decourchelle, A. 2003, A&A, 407, L17
Portegies Zwart, S., Gaburov, E., Chen, H.-C., & Gürkan, M. A. 2007, MNRAS, 378, L29
Portegies Zwart, S. F., Baumgardt, H., Hut, P., Makino, J., & McMillan, S. L. W. 2004, Nature, 428, 724
Portegies Zwart, S. F., & McMillan, S. L. W. 2002, ApJ, 576, 899
Reid, M. J. 1993, ARA&A, 31, 345
Reid, M. J., & Brunthaler, A. 2004, ApJ, 616, 872
Rieke, G. H., & Lebofsky, M. J. 1985, ApJ, 288, 618
Rieke, M. J. 1999, in Astronomical Society of the Pacific Conference Series, Vol. 186, The Central Parsecs of the Galaxy, ed. H. Falcke, A. Cotera, W. J. Duschl, F. Melia, & M. J. Rieke, 32–+
Rousset, G., et al. 2003, in Presented at the Society of Photo-Optical Instrumentation Engineers (SPIE) Conference, Vol. 4839, Adaptive Optical System Technologies II. Edited by Wizinowich, Peter L.; Bonaccini, Domenico. Proceedings of the SPIE, Volume 4839, pp. 140-149 (2003)., ed. P. L. Wizinowich & D. Bonaccini, 140–149
Schödel, R., Eckart, A., Iserlohe, C., Genzel, R., & Ott, T. 2005, ApJ, 625, L111

Schödel, R., et al. 2002, Nature, 419, 694
Schoedel, R., Najarro, F., Muzic, K., & Eckart, A. 2009, ArXiv e-prints
Trippe, S., Davies, R., Eisenhauer, F., Foerster Schreiber, N. M., Fritz, T. K., & Genzel, R. 2009, ArXiv e-prints
Trippe, S., et al. 2008, A&A, 492, 419

Wang, Q. D., Lu, F. J., & Gotthelf, E. V. 2006, MNRAS, 367, 937
Zhao, J.-H., & Goss, W. M. 1998, ApJ, 499, L163+
Zhao, J.-H., Morris, M. R., Goss, W. M., & An, T. 2009, ApJ, 699, 186

APPENDIX

A: OBTAINING THE SEDS

Deconvolution of SINFONI data

In order to distinguish between objects in the SINFONI data, we deconvolve the cube in small bandpasses, taking into account the variation of the PSF with wavelength. We extract line maps at three wavelengths at which single stars prominently dominate the respective images: at $1.49\,\mu$m the dominant star is E4, at $1.70\,\mu$m and $2.11\,\mu$m it is E2. We manually remove apparent artifacts and smooth the PSF wings azimuthally. We then spectrally interpolate and extrapolate these single-wavelength PSFs over the whole wavelength range, either resampled to 24 spectral channels or at the original spectral sampling. We then used two sets of PSFs to perform deconvolution of the cube at the different samplings. We use the deconvolution at the original sampling for extracting the spectra of the WR stars E2 and E4.0. The resampled deconvolution is used for E3.0 and 5.0.

We also use the PSFs interpolated at originally sampling for creating a subtracted cube in which the four brightest stars (E1, E2, E4.0 and the bright late-type star north-west of IRS13E) are subtracted. For this purpose we fit in each spectral plane the stars with Gaussians to determine their flux as a function of wavelength. Then we subtract the correspondingly scaled, interpolated PSFs from the original data cube. We use the resulting cube for analyzing the spectral features of the gas and the fainter stars.

We flux-calibrate the SINFONI data by using the early-type star E1, in the spectrum of which we manually replace the (few) spectral lines by continuum. The photometric errors from the SINFONI data are estimated by varying the selection of source pixels. During the fit, we rescale them such that the reduced $\chi^2 = 1$.

Photometry from NACO images

In order to measure the SED of the objects fainter or more confused than E5.0, we determine fluxes from the deconvolved broad-band and narrow-band images. We measure the flux of each object at each available wavelength by manually selecting the respective object pixels in the frames. For the broad-band images we estimate the flux errors from the standard deviation of the measured fluxes at the different epochs. For the narrow-band images we simply adopt the same flux errors as obtained from the broad-band images.

For the broad-band images in H and Ks, we calibrate the magnitudes following Maness et al. (2007)[8]. We derive the narrow-band calibration from the broad-band calibration by using the empirical extinction law

$$A_\lambda = A_{\rm Ks} * \lambda/\lambda_{\rm Ks}{}^\alpha = A_{\rm Ks} * \lambda/\lambda_{\rm Ks}{}^{-1.75} \tag{A1}$$

from Draine (1989). As calibrators we use eight isolated, bright early-types stars with known temperatures within a distance of less than 2.5" to IRS13E. Since there is no suitable L'-band calibrator close to IRS13E, we use an indirect method by extrapolating the dereddened SED of the calibrators to L'-band and applying the extinction law from Lutz et al. (1996) longward of Brackett-β and short-ward the power law of Draine (1989). This results in $A_{\rm Ks}/A_{\rm L'} = 1.75$. The slope of the power law in equation A1 is uncertain: $\alpha = -1.6$ (Rieke & Lebofsky 1985; Rieke 1999), $\alpha = -2$ (Nishiyama et al. 2009) and $\alpha = -2.21$ (Schoedel et al. 2009). At our precision the uncertainty of α does not affect the indirectly calibrated bands and consequently the shape of the derived SED is relatively insensitive to the value of α adopted. But it introduces an uncertainty to the extinction values. Together with the uncertainty of the absolute calibration the assumed magnitudes of the objects could be up to 0.4 mag brighter or up to 0.8 mag fainter.

For the SED fits, we calculate the effective wavelength of the bands for each object. First, we apply an extinction value of $A_{\rm Ks} = 2.8$ together with the atmospheric and the filter transmission to the source spectrum (either a blackbody of the output from the atmosphere modeling). For the broad-band data it is necessary to perform a second iteration using the resulting SED in order to improve the effective wavelength.

B: INDIVIDUAL OBJECTS IN IRS13E

IRS13E1

E1 is a hot OB supergiant (Paumard et al. 2006). Its flux is constant in our data, and the spectrum does not reveal any signs of binarity. We use the H-band lines from the Brackett-series to determine the radial velocity (in K-band, the emission lines from nebular background are more dominant). We obtain $v_{\rm LSR} = 134 \pm 10$ km/s. This is 3σ different to $v_{\rm LSR} = 71 \pm 20$ km/s, the Brackett-γ based value reported in Paumard et al. (2006).

We compare our atmosphere model of E1 to a simple blackbody model of $T = 27500$ K and do not see differences between the two models which would matter for the broad-band photometry. Therefore, we fit the extinction using

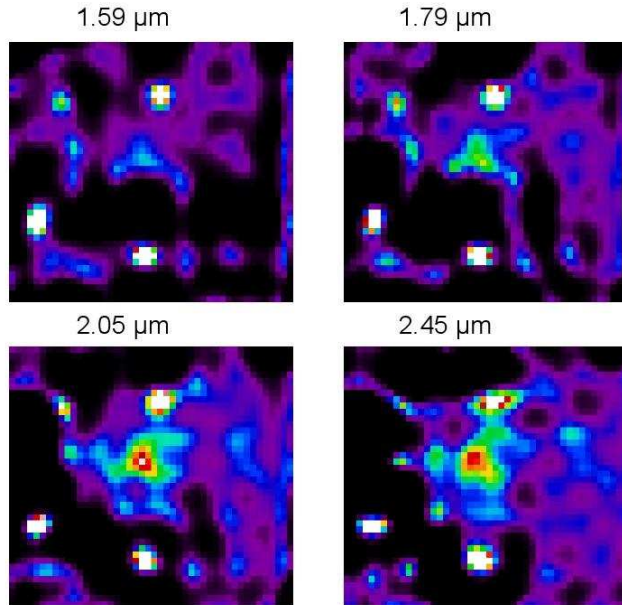[8] The calibration of Schoedel et al. (2009) is about 0.3 mag fainter in both bands.

FIG. 11.— Four of the 24 deconvolved narrowband images created from the high-quality H+K-band SINFONI cube of IRS13E.

the photometric data and a blackbody model. We obtain $A_{\mathrm{Ks}} = 3.64 \pm 0.07$ (figure 4). Contrary to Maillard et al. (2004), we do not find a weak dust component. This is likely because of the higher resolution of our data, since the SINFONI data show that the star is surrounded by gas probably also associated with dust.

IRS13E2

E2 is a Wolf-Rayet star of type WN8 (Paumard et al. 2006; Martins et al. 2007). There is no sign of binarity in the photometric light curve or in its spectrum. The latter shows strong, broad emission lines. In addition, WR-stars have strong winds causing a near-infrared excess. Therefore it is necessary to use a full atmosphere model for the SED fit of E2. We manually adjust the temperature of a possible dust component and the extinction parameter to make the atmosphere model match the observed spectrum.

The SED fit yields a second blackbody component of around $T = 712\,\mathrm{K}$ and $A_{\mathrm{Ks}} = 3.51$. This result is qualitatively consistent with the findings of Maillard et al. (2004). The smaller dust temperature they find is likely caused by their assumption that E2 can be modeled with a blackbody. We find that the dust component is significant in L'-band, but in Ks-band the stellar component dominates (see Figure 2), contrary to the proposal by Martins et al. (2007).

E2 appears to be intrinsically quite bright with $\log L/L_\odot = 6.14^{+0.16}_{-0.32}$ for its classification as WN8 star. Thus, E2 could be more massive and even younger ($\approx 3\,\mathrm{Myr}$) than most of the young, massive stars in the central parsec. However, due to the particular shape of the evolutionary tracks, E2 could equally well have the same age as the other stars of similar type. The fact that E2 is brighter than the other WN8 stars in the GC is unaffected by calibration uncertainties. Also, binarity would not be able to fully explain the luminosity of E2.

We use the full atmosphere model for deriving the radial velocity of E2, which is more accurate compared to previous works. We obtain $v_{\mathrm{LSR}} = 65 \pm 30\,\mathrm{km/s}$ from the 2.24 μm NIII line while Paumard et al. (2006) reported $v_{\mathrm{LSR}} = 40 \pm 40\,\mathrm{km/s}$ and Maillard et al. (2004) gave $v_{\mathrm{LSR}} = 30\,\mathrm{km/s}$. All these values are consistent with each other.

IRS13E3.1 to IRS13E3.4

The extracted PSFs of the SINFONI data are not good enough to measure the H-band part of the SEDs of the fainter objects around E3.0. Qualitatively, the spectra of E3.1 to E3.4 do not show any new spectral features compared to E3.0. There is only a gradual change in the spectral properties, such as the line velocities. Hence, these sources also likely consist mostly of gas and dust. This is confirmed by the SED fits, which are based on the narrow-band images. Because of the faintness of the sources we cannot reliably fit the extinction, which we restrict for pure dust sources to $A_{\mathrm{Ks}} = 3.4 - 3.9$.

On most images in K-band (including the narrow-band images before 2005) and all L'-band data, the sources E3.1 and E3.2 are strongly overlapping. Therefore we fit a combined SED for the two (Figure 4). The properties of the fitted blackbody are similar to E3.0 apart from its brightness. A stellar component is not necessary, the 1σ limit is $m_{\mathrm{Ks}} = 18.0$, and thus again we can exclude that a WR star of the most common types is hidden in E3.1 and E3.2. We suspect that Maillard et al. (2004) found a stellar component in the eastern part of their source E3 due to the same bias as for E3.0 (section 4.2.1). Also for the less well constrained objects E3.3 and E3.4 (table 2) no stellar components are required. This conclusion does not depend on the assumption for the extinction.

IRS13E3.5

The SED of E3.5, derived photometrically, differs from the other sources in E3 (figure 4). Its color is consistent with that of a star, and no dust is necessary to explain the SED of this object. Unfortunately, it is too confused and too faint for deriving its spectral type. Any temperature between $4000\,\mathrm{K}$ and $19000\,\mathrm{K}$ is possible, which also implies an uncertainty of $\Delta A_{\mathrm{Ks}} = 0.4$. The absolute magnitude of E3.5 corresponds to the red clump, which makes it likely that E3.5 is an old, late-type star. In addition, this star does not share the proper motion of the three brightest stars in IRS13E. We conclude that E3.5 most likely does not belong to IRS13E.

IRS13E4.0

E4 is a Wolf-Rayet (WC9) star (Paumard et al. 2006; Martins et al. 2007). Its radial velocity is very uncertain. Paumard et al. (2006) report $v_{\mathrm{LSR}} = 56\pm70\,\mathrm{km/s}$, Maillard et al. (2004) claim $v_{\mathrm{LSR}} = -30\,\mathrm{km/s}$. From our atmosphere model (figure 2) that includes the wind induced line broadening we obtain $v_{\mathrm{LSR}} = 200 \pm 200\,\mathrm{km/s}$.

As for E2 we manually adjust the atmosphere model with an additional dust component to match the measured spectrum (figure 2). Two blackbodies are needed to describe the SED. The dust component with $T = 1400\,\mathrm{K}$ is significant. It contributes 38% of the flux in the Ks-band, as indicated by Martins et al. (2007). Our measurement is more precise than the one from Maillard et al. (2004), because we use a full atmosphere model and extend the wavelength coverage to L'-band. We obtain the same extinction as for E1. The luminosity of E4 is $\log L/L_\odot = 5.23^{+0.16}_{-0.32}$, which is similar to the other WC9 stars in the GC (Martins et al. 2007). We conclude that E4.0 likely has the same age as the other young, massive stars in the GC.

IRS13E4.1 to IRS13E4.3

Besides H- and Ks-band, E4.1 is detected also in L'-band and has overall a red SED. It is too close to E4.0 to allow the broadband SED to be extracted from the SINFONI data. The spectrum shows only gas lines and no stellar features. For fitting the SED it was necessary to fix the extinction at the upper end of the possible range to $A_{\mathrm{Ks}} = 3.9$. With this the data are fit well by a single blackbody of $T = 844 \pm 24\,\mathrm{K}$. Any stellar component has to be fainter than $m_{\mathrm{Ks}} = 18.4$.

E4.2 does not show any spectral features and is not detected in L'-band. Therefore, there is less data than for the previous sources. We fix $A_{\mathrm{Ks}} = 3.9$. From a single blackbody fit we get a temperature of less than $2800\,\mathrm{K}$, which is too cold for a star of $m_{\mathrm{Ks}} = 15.4$. Thus, we need to add a second blackbody to the fit, which means we classify E4.2 as a star. As in the case for E3.5, this faint star matches the typical luminosity of red clump stars. Hence, it is most likely an old late-type star. Its motion, being slower westward than for the three bright stars in IRS13E, argues against E4.2 being a physical member of IRS13E.

For E4.3 we are only able to photometry in Ks-band, yielding $m_{\mathrm{Ks}} = 15.5 \pm 0.1$.

IRS13E5.0

The source E5.0 is isolated enough for us to extract its broadband SED in the Ks-band from the SINFONI data (figure 4), but because of its location close to the edge of the data cube, the SINFONI H-band measurements are not reliable. Hence, we combine the NACO-based fluxes with the SINFONI data. We allow for a global scaling factor to match the two data sets, which yields an offset of $0.24\,\mathrm{mag}$. In any case, the fit does not change significantly by either including or excluding the SINFONI data. The preferred fit yields $A_{\mathrm{Ks}} = 3.22$ and a dusty blackbody. Thus, we fix the extinction value to the lowest value from the range assumed here to $A_{\mathrm{Ks}} = 3.4$. Again, no stellar component is needed, and any star inside is fainter than $m_{\mathrm{Ks}} = 18.5$. The dust of E5.0 is with $T = 700 \pm 8\,\mathrm{K}$ colder than for most other objects in E3 and E4. Maillard et al. (2004) were only able to identify one source in E5. The scatter in their data points is so high that it is not clear how significant the stellar component is in their fits.

IRS13E5.1 to IRS13E5.4

The other sources of E5 are also red but fainter than E5.0. They appear embedded in the brightest part of the minispiral. It is not possible to measure their SEDs separated from the minispiral at our resolution, because the background is inhomogeneous and therefore the background subtraction too uncertain. subtraction is too uncertain given the inhomogeneous background. This holds both for the NACO photometry and for the SINFONI data. In addition, the sources E5.2 and E5.3 are located on the deconvolution ring of the bright source E1. Thus, the fluxes of these two sources are biased to high values, especially in H-band. Finally many of the objects are not detected in all our NACO bands. Consequently, the characterization of these source is considerably more uncertain than for the other sources. The spectra of these sources show only gaseous emission lines. We again assume that the continuum emission is mainly caused by dust, and thus we restrict A_{Ks} to the range $3.4 - 3.9$.

The source E5.1 is a double source on the higher quality Ks-band images obtained since 2008, but we are not yet able to disentangle them. This source is also detected in the L'-band. With our assumption for the extinction, the best fit is a blackbody with $T = 947 \pm 25\,\mathrm{K}$; any stellar component needs to be fainter than $m_{\mathrm{Ks}} = 17.8$.

The source E5.2 is not detected in H-band but in L'-band, where it is nearly overlapping with E5.3. We nevertheless simply assume that all of the L'-flux is caused by E5.2. With this we obtain a temperature of $T = 642 \pm 70\,\mathrm{K}$ from the SED fit, which is consistent with the non-detection in the H-band. Any star hidden in E5.2 must be fainter than $m_{\mathrm{Ks}} = 15.6$. Given the lower temperature, E5.2 is likely a part of the minispiral.
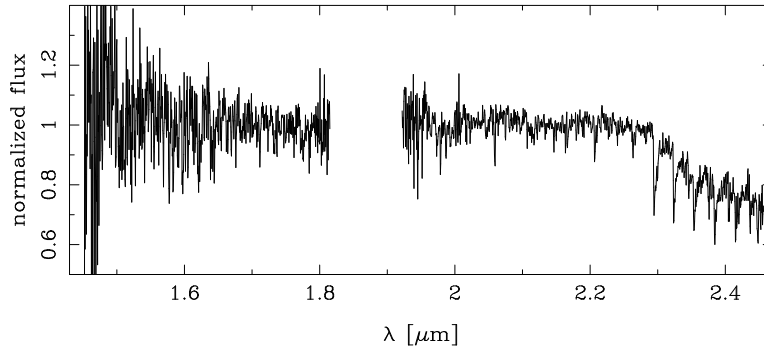
Fig. 12.— SINFONI H+K-band spectrum of E6.

Contrary to E5.2, the object E5.3 is not detected in L'-band but in H-band. Our fit does not require a stellar component. The 1σ-limit is $m_{\mathrm{Ks}} = 16.0$ and we obtain a temperature of $T = 978 \pm 524\,\mathrm{K}$. The large error is caused by the smaller wavelength range on which the SED fit is based.

The source E5.4 is located close to E5.0. It is detected only in Ks- and the narrow bands. Hence we fit only a single blackbody with the restricted extinction interval. We obtain a temperature of $T = 817 \pm 474\,\mathrm{K}$.

IRS13E6

The spectrum (figure 12) of E6 ($m_{\mathrm{Ks}} = 13.82 \pm 0.10$) shows CO-band heads in H- and Ks-band and lines of NaI and CaI. Thus, E6 is a late-type star with a spectral class around K3III. Maillard et al. (2004) identified E6 as an O-star, but they used data from three relatively broad bands for their photometric identification. Buchholz et al. (2009) used narrow bands around the CO-band heads and determined correctly that E6 is a late-type star. We derive a radial velocity of $v_{\mathrm{LSR}} = 106 \pm 10\,\mathrm{km/s}$ from the CO-band heads in Ks-band.

In order to avoid biases, we exclude from the SED fit the bands which contain flux of the CO band heads. The fitted extinction value of $A_{\mathrm{Ks}} = 3.68 \pm 0.09$ is consistent with the extinction of E1. Due to its faintness E6 cannot be a red supergiant and it is thus older than the three bright early-type stars.
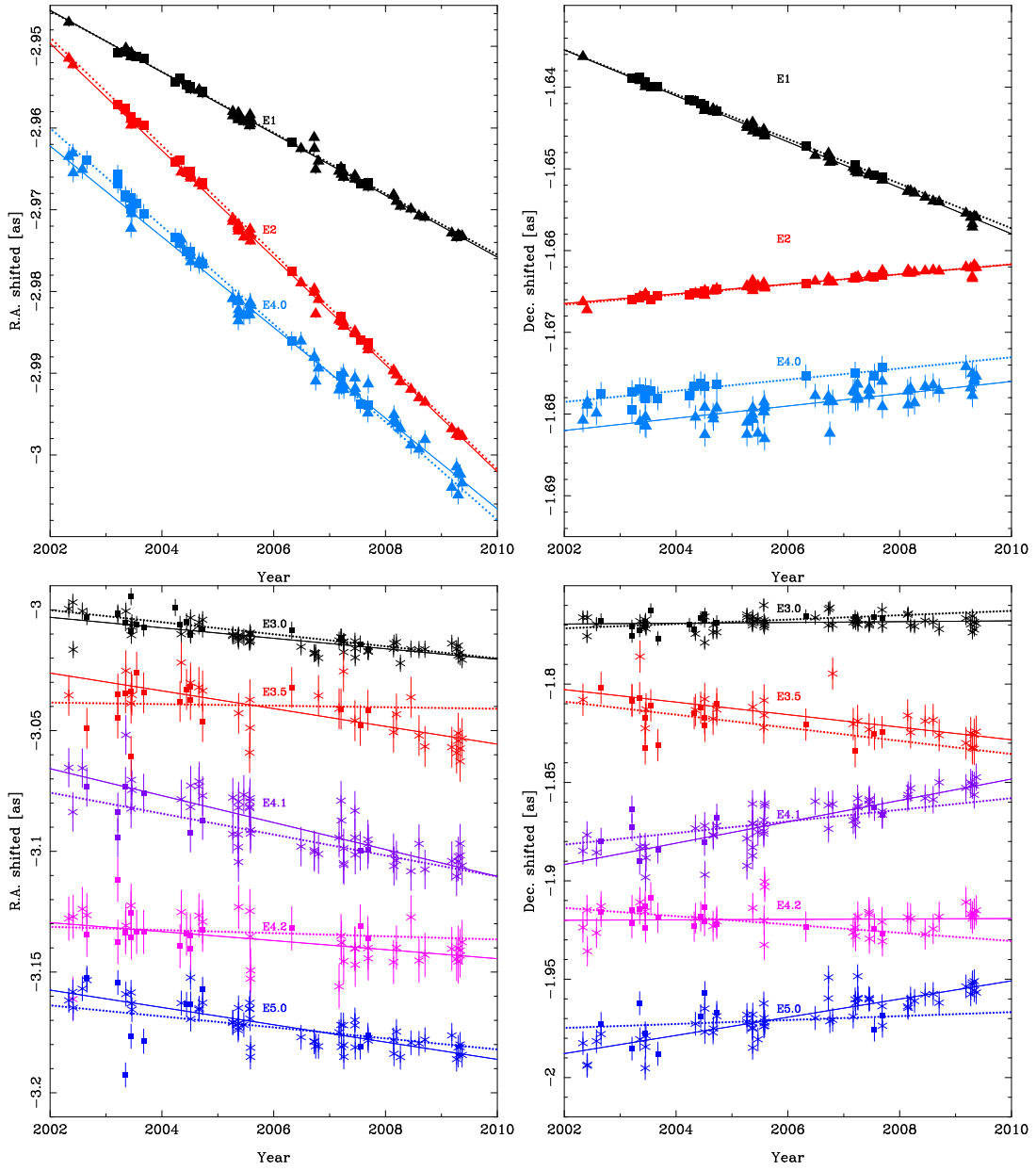
C: ASTROMETRIC DATA

FIG. 13.— Positions and linear motion fits for the objects in IRS13E. Top: The three bright stars in Ks-band (asterisks and solid lines) and H-band (boxes and dotted lines). Bottom: Some of the fainter objects. All data and fits are offset from each other for clarity.